

UC Berkeley

UC Berkeley Previously Published Works

Title

Plasmon-Enhanced Photocatalytic CO₂ Conversion within Metal–Organic Frameworks under Visible Light

Permalink

<https://escholarship.org/uc/item/4ng1q3z2>

Journal

Journal of the American Chemical Society, 139(1)

ISSN

0002-7863

Authors

Choi, Kyung Min
Kim, Dohyung
Rungtaweeveranit, Bunyarat
[et al.](#)

Publication Date

2017-01-11

DOI

10.1021/jacs.6b11027

Peer reviewed

Plasmon-Enhanced Photocatalytic CO₂ Conversion within Metal-Organic Frameworks Under Visible Light

Kyung Min Choi^{†,§,▽,#}, Dohyung Kim^{‡,#}, Bunyarat Rungtaweevoranit^{†,§}, Christopher A. Trickett^{†,§}, Jesika Trese Deniz Barmanbek[†], Peidong Yang^{*,†,‡,§,||}, Omar M. Yaghi^{*,†,§,||,Δ}

[†]Department of Chemistry, [‡]Department of Materials Science and Engineering, University of California–Berkeley;

[§]Materials Sciences Division, Lawrence Berkeley National Laboratory; ^{||}Kavli Energy NanoSciences Institute at Berkeley; and ^ΔGlobal Science Institute at Berkeley, Berkeley, California 94720, United States

[▽]Department of Chemical and Biological Engineering, Sookmyung Women's University, Seoul 04310, Korea

^ΔKing Abdulaziz City for Science and Technology, Riyadh, Saudi Arabia

ABSTRACT: Materials development for artificial photosynthesis, in particular CO₂ reduction, has been under extensive efforts, ranging from inorganic semiconductors to molecular complexes. In this report, we demonstrate a metalorganic framework (MOF) coated nanoparticle photocatalyst with enhanced CO₂ reduction activity and stability, which stems from having two different functional units for activity enhancement and catalytic stability combined together as a single construct. Covalently attaching a CO₂-to-CO conversion photocatalyst Re^I(CO)₃(BPYDC)Cl, BPYDC = 2,2'-bipyridine-5,5'-dicarboxylate, to a zirconium MOF, UiO-67 (Re_n-MOF), prevents dimerization leading to deactivation. By systematically controlling its density in the framework (n = 0, 1, 2, 3, 5, 11, 16, and 24 complexes per unit cell), the highest photocatalytic activity was found for Re₃-MOF. Structural analysis of Re_n-MOFs suggest that a fine balance of proximity between photoactive centers is needed for cooperatively enhanced photocatalytic activity, where an optimum number of Re complexes per unit cell should reach the highest activity. Based on the structure-activity correlation of Re_n-MOFs, Re₃-MOF was coated onto Ag nanocubes (Ag@Re₃-MOF), which spatially confined photoactive Re centers to the intensified near-surface electric fields at the surface of Ag nanocubes, resulting in a seven-fold enhancement of CO₂-to-CO conversion under visible light with long-term stability maintained up to 48 hours.

INTRODUCTION

Inorganic nanostructures and molecular complexes have been widely investigated as artificial photosynthetic catalysts^{1,2}. The challenge is to find catalysts for carbon dioxide reduction with good activity, selectivity and durability, especially under visible light. In this context, metal-organic frameworks (MOFs) offer many advantages because of the flexibility with which they can be designed and their pore environment varied³.

Here, we demonstrate how tunable photocatalytic activity can be realized by quantitatively and precisely controlling the density of covalently attached photoactive centers within MOF interior, and how this prevents the dimerization of the molecular catalyst and its deactivation. Furthermore, for the first time, these MOF catalytic units can be spatially localized within the enhanced electromagnetic field surrounding plasmonic silver nanocubes to significantly increase their photocatalytic activity for carbon dioxide conversion under visible light⁴. Specifically, we covalently attached Re^I(CO)₃(BPYDC)(Cl), BPYDC = 2,2'-bipyridine-5,5'-dicarboxylate [hereafter referred to as ReTC],

within a zirconium MOF based on the UiO-67-type structure⁵ (hereafter this Re containing MOF is termed Re_n-MOF) and controlled its density in the pores in successive increments of n (n = 0, 1, 2, 3, 5, 11, 16, and 24 complexes per unit cell), finding the highest activity for n = 3 complexes. The effect of the molecular environment within MOFs for photocatalytic CO₂ reduction was studied, which provided further insights into the photocatalytic reaction pathway of molecular Re complex. Placing this construct on silver nanocubes resulted in seven-fold enhancement of carbon dioxide photocatalytic conversion to carbon monoxide.

Many studies involving the use of photoactive metal complexes^{1,6}, MOFs^{7,8}, and inorganic nanostructures⁹ for carbon dioxide reduction have been reported with varying levels of performance. The present catalysts' unique performance is attributed to the precision and systematic variation applied in their design, and the spatial resolution with which they can be interfaced with plasmonic nanostructures.

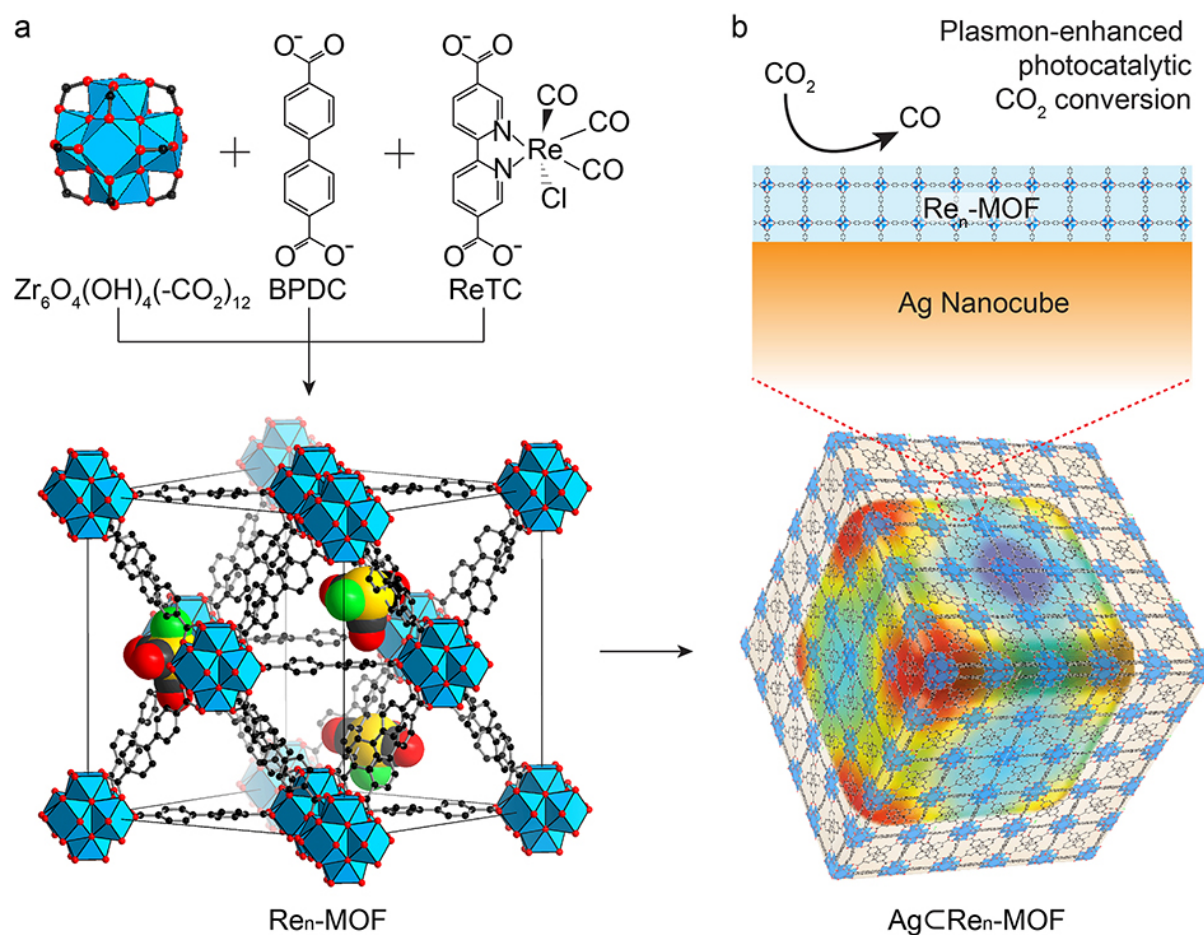


Figure 1. Structures of $\text{Re}_n\text{-MOF}$ and $\text{Ag@Re}_n\text{-MOF}$ for plasmon-enhanced photocatalytic CO_2 conversion. (a) $\text{Zr}_6\text{O}_4(\text{OH})_4(-\text{CO}_2)_{12}$ secondary building units (SBUs) are combined with BPDC and ReTC linkers to form $\text{Re}_n\text{-MOF}$. The structure of $\text{Re}_3\text{-MOF}$ identified from single crystal X-ray diffraction is shown. 12-coordinated Zr-based metal clusters are interconnected by 21 BPDC and 3 ReTC linkers in a face-centered cubic array. Atom labeling scheme: C, black; O, red; Zr, blue polyhedra; Re, yellow; Cl, green, H atoms are omitted for clarity. (b) $\text{Re}_n\text{-MOF}$ coated on a Ag nanocube for enhanced photocatalytic conversion of CO_2 .

EXPERIMENTAL SECTION

Synthesis of $\text{Re}(\text{CO})_3(\text{H}_2\text{BPYDC})\text{Cl}$, H_2ReTC : $\text{Re}(\text{CO})_5\text{Cl}$ (0.360 g, 1.000 mmol) and H_2BPYDC (0.240 g, 1.000 mmol) were added to methanol (100 mL). After refluxing the mixture for 24 h under N_2 , the resultant precipitate was filtered and the solvent was evaporated under reduced pressure to give the product. $^1\text{H NMR}$ ($\text{DMSO}-d_6$): 9.35 (s, 2H), 9.01 (d, 2H), 8.79 (d, 2H).

Synthesis of $\text{Re}_n\text{-MOFs}$: Different ratios of H_2ReTC and H_2BPDC (0, 5, 10, 20, 30, 50, 70, and 100 mol% of H_2ReTC , adding up to a total amount of 0.040 mmol of organic linker) were mixed with 10 ml DMF solution containing ZrCl_4 (9.320 mg, 0.040 mmol) and acetic acid (0.5 ml, 8.7 mmol) in a 20 ml vial, which was heated at 100 °C for 10 h. An orange precipitate was collected and washed three times with DMF using a centrifuge (9000 rpm for 10 min)

and sonication, and then sequentially immersed in anhydrous acetonitrile for three 24 h periods.

Synthesis of Ag nanocube: Silver nitrate (0.25 g) and copper(II) chloride (0.21 mg) were dissolved in 1,5-pentanediol (12.5 mL) in a 20 ml glass vial. In a separate vial, PVP ($M_w = 55,000$, 0.25 g) was dissolved in 1,5-pentanediol (12.5 mL). Using an oil bath, 1,5-pentanediol (20 mL) was heated for 10 min at 190 °C. Then the two precursor solutions were injected at different intervals: 500 μL of the silver nitrate solution every minute and 250 μL of the PVP solution every 30 s. The reaction was stopped once the solution turned opaque (~7 min).

Synthesis of $\text{Ag@Re}_3\text{-MOF}$: Ag nanocubes were washed three times with DMF using a centrifuge (9000 rpm for 10 min) and concentrated to a 3 mg/ml Ag nanocube solution. A Re-MOF stock solution was prepared by dissolving H_2BPDC (9.110 mg, 0.037 mmol), H_2ReTC (1.320 mg, 0.002

mmol), $ZrCl_4$ (9.32 mg, 0.04 mmol), and acetic acid (0.500 ml, 8.700 mmol) in 10 ml DMF. Then 2.1 ml of the Re-MOF stock solution and 2 ml of the Ag nanocube solution were combined with 1 ml DMF containing 0.125 ml acetic acid in a 20 ml vial with a magnetic stirrer and heated at 90 °C in an aluminum heating block with vigorous stirring. The thickness of the Re-MOF layer could be controlled with reaction time; $Ag@Re_3$ -MOF-16nm and -33nm was synthesized after 25 and 30 min, respectively. The precipitate was collected and washed three times with DMF using a centrifuge (9000 rpm for 10 min) and sonication, then sequentially immersed in anhydrous acetonitrile for three 24 h periods.

Photocatalytic experiments. The experiments were performed in a sealed batch-type custom cell. Samples were dispersed in acetonitrile (20 ml) with 1 ml triethylamine added as a sacrificial electron donor. Initially, the cell was purged with CO_2 for 20 min and then sealed at 1 atm CO_2 . A 300W Xe lamp with visible band-pass filters was used so that the light contained regions in wavelength be-

tween 400 to 700 nm. The amount of Re tricarbonyl complex in each sample was 0.5 ~ 8 μ mol, depending on the degree of ReTC incorporation inside MOFs while the nanocrystal number per volume was kept similar. The products were measured by injecting 1 ml of gas in the headspace to a gas chromatograph (SRI) after every 1 or 2 hour run.

Characterization. Powder X-ray diffraction patterns (PXRD) were recorded using a Bruker D8 Advance diffractometer (Göbel-mirror monochromated $Cu K\alpha$ radiation $\lambda = 1.54056 \text{ \AA}$). Gas adsorption analysis was performed on a Quantachrome Quadrasorb-SI automatic volumetric gas adsorption analyzer. A liquid nitrogen bath (77 K) and ultra-high purity grade N_2 and He (99.999%, Praxair) were used for the measurements. Samples were prepared and measured after evacuating at 100 °C for 12 h. For transmission electron microscopy (TEM) observation, samples were first dispersed in an organic solvent by sonication and dropped onto a TEM grid. TEM was carried out at 200 kV using a JEOL JEM-2100. The amount of Re complexes in Re_n -MOFs was analyzed by an ICP-AES spectroscope (Op-

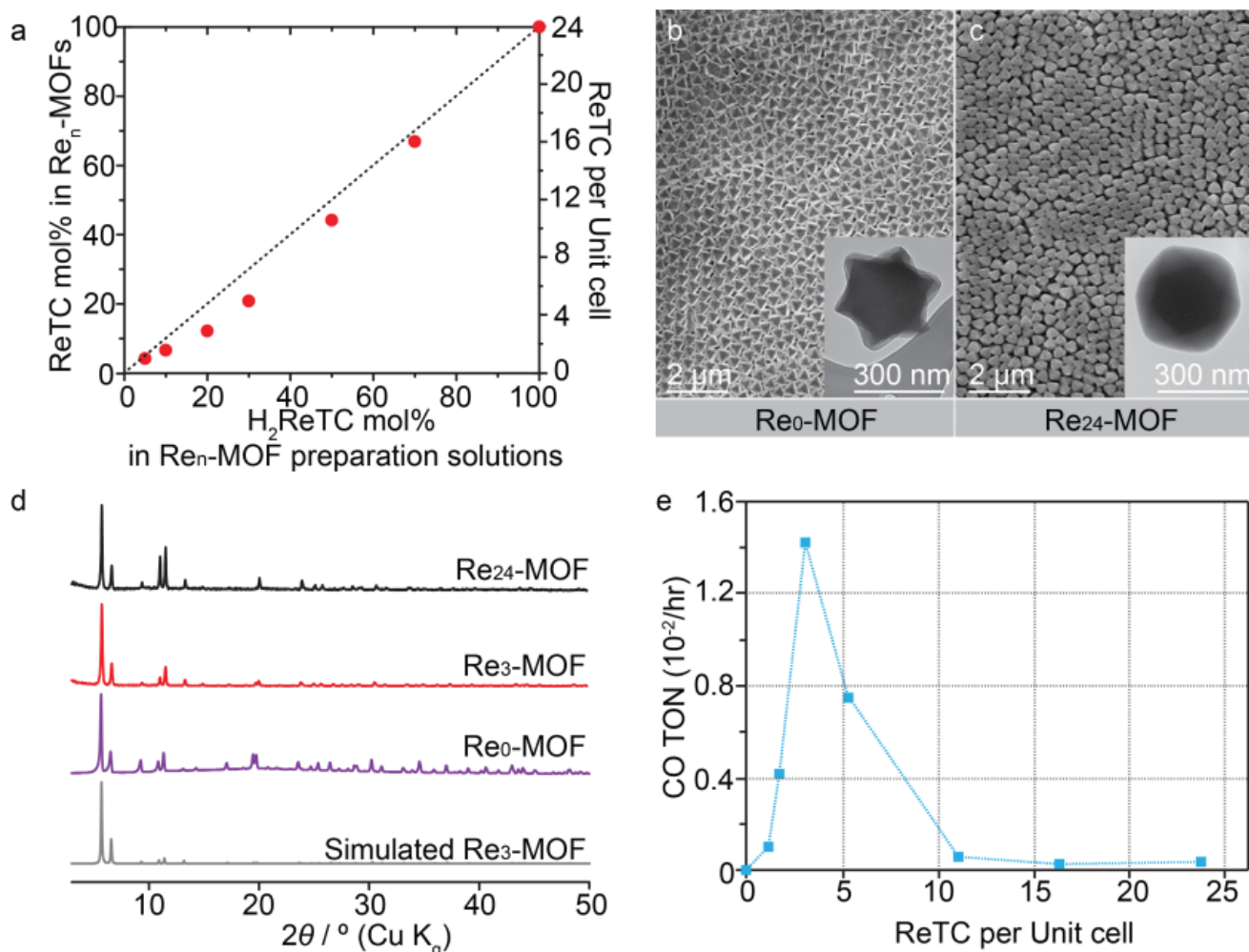


Figure 2. Characterization and photocatalytic activity of Re_n -MOFs. (a) Percent incorporation of ReTCs in Re_n -MOFs. SEM images of (b) Re_0 - and (c) Re_{24} -MOFs. Insets are TEM images of each. (d) PXRD patterns of Re_n -MOFs in comparison with the simulated pattern of Re_3 -MOF. (e) Photocatalytic CO_2 -to- CO conversion activity under visible light (400 – 700 nm).

tima 7000 DV, Perkin Elmer). Samples (10 mg) were digested using a mixture of nitric acid (0.5 ml), hydrochloric acid (1.5 ml) and hydrofluoric acid (30 μ l) and then diluted with 2 vol% of nitric acid solution (10 ml) before measurement. For NMR, 10 mg of dried sample was digested and dissolved by sonication in a mixture of DMSO- d_6 (1 ml), hydrofluoric acid (20 μ l) and D $_2$ O (20 μ l). The digested solution was used directly for 1 H NMR. Attenuated total reflectance (ATR) FTIR spectra of neat samples was performed on a Bruker ALPHA Platinum ATR-FTIR Spectrometer equipped with a single reflection diamond ATR module. Liquid samples were measured by placing a sample droplet on the sample stage covered with a cap for preventing solvent evaporation.

RESULTS AND DISCUSSION

1. Structural Analysis and Photocatalytic Activity of Re $_n$ -MOFs

Structural Analysis of Re $_3$ -MOF. The structural determination of Re $_3$ -MOF was carried out by single crystal X-ray diffraction (Figure 1). Single crystals of Re $_3$ -MOF were prepared by dissolving the protonated form of H $_2$ ReTC (20 mol%), H $_2$ BPDC (80 mol%, BPDC = 4,4'-biphenyldicarboxylate), and ZrOCl $_2$ ·8H $_2$ O in a solution mixture of DEF/formic acid in a 20 ml screw-capped vial and heating at 140 $^{\circ}$ C for 12 h [Figure S1 in Supporting Information (SI)]. The analysis of single-crystal X-ray diffraction data reveals that Re $_3$ -MOF crystallizes in the cubic $Fm\bar{3}m$ space group with unit cell parameter $a = 26.7213(8)$ \AA (Supporting Information Table 1 and Figure 2). Each Zr secondary building unit, Zr $_6$ O $_4$ (OH) $_4$ (-CO $_2$) $_2$, is coordinated to a total of 12 linkers (ReTC and BPDC) resulting in a three-dimensional **fcu** network. Inductively coupled plasma atomic emission spectroscopy (ICP-AES) analysis performed on these crystals gave a molar ratio of 0.12 mol of Re to 1 mol Zr. This corresponds to 3 ReTCs per unit cell (i.e. Re $_3$ -MOF), as confirmed by the X-ray structure of single crystalline Zr $_6$ O $_4$ (OH) $_4$ [Re(CO) $_3$ (Cl)-BPYDC] $_{0.72}$ (BPDC) $_{5.28}$, where covalently bound ReTCs are found in octahedral cavities of face centered cubic arrangement. Moreover, chloride occupies the axial position and was refined from the Fourier difference map, indicating *fac*-arrangement of the ReTC in Re $_3$ -MOF, which is an identical geometry compared to that of the mononuclear Re-complex in solution 10 (Figure S2 in SI).

The *fac*-arrangement of ReTC in Re $_3$ -MOF is also supported by infrared (IR) spectroscopy (Figure S3 in SI), ultraviolet-visible (UV-Vis) spectroscopy (Figure S4 in SI), and 1 H nuclear magnetic resonance (NMR) spectra (Figure S5 in SI). The IR spectrum of Re $_3$ -MOF was measured in powder form and ν (CO) bands were observed at 2,022, 1,920, and 1,910 cm^{-1} (Figure S3 in SI), consistent with the *fac*-isomer of molecular ReTC 10 . The UV-Vis spectrum, measured as a powder mixed with KBr, has a metal-to-ligand and charge transfer (MLCT) absorption band at 400 nm, indicative of the *fac*-isomer of ReTC 10 (Figure S4 in SI). The

amount of ReTC in the MOF and its molecular configuration were further confirmed from 1 H NMR of a HF-digested solution of Re $_3$ -MOF (Figure S5 in SI).

ReTC Density Varied in Re $_n$ -MOFs. To examine how the amount of ReTC in MOFs affects the structural environment within the MOF interior for CO $_2$ catalytic turnover, the ReTC density was varied in the range from Re $_0$ -MOF (ReTC free MOF) to Re $_{24}$ -MOF (ReTC at maximal loading). This was done by adding increasing amounts of H $_2$ ReTC to the total amount of organic linkers during MOF synthesis, which resulted in Re $_n$ -MOFs ($n = 0, 1, 2, 3, 5, 11, 16, \text{ and } 24$) identified from ICP-AES (Figure 2a). All samples were synthesized as monocrystalline nanoparticles (Figure S6-8 in SI) as this may facilitate diffusion of substrates and products to and from the active Re catalytic centers. Representative scanning electron microscopy (SEM) images (Figures 2b and c, and Figure S7 in SI) of Re $_n$ -MOFs show great size uniformity (*ca.* 300 nm) and identical octahedral geometry of particles regardless of the amount of ReTC incorporated. The crystallinity of Re $_n$ -MOFs was examined by powder X-ray diffraction (PXRD) (Figure 2d and Figure S8 in SI), which gave sharp diffraction lines matching those of the simulated pattern obtained from experimental single crystal X-ray diffraction data of Re $_3$ -MOF. This clearly indicates preservation of the single crystalline Re $_3$ -MOF structure upon introduction of different density of ReTC in Re $_n$ -MOFs. The permanent porosity of all Re $_n$ -MOF samples was confirmed by measurement of their N $_2$ sorption isotherms (Figure S9 in SI). UV-Vis spectroscopy for all Re $_n$ -MOFs showed that the MLCT absorption band intensities increase as more ReTCs are incorporated into the framework, further confirming the varied density of the photoactive units in Re $_n$ -MOFs (Figure S10 in SI).

Photocatalytic CO $_2$ Conversion for Re $_n$ -MOFs. All Re $_n$ -MOFs used for photocatalytic CO $_2$ conversion were dispersed in acetonitrile/triethylamine mixture (MeCN : TEA = 20 : 1) saturated with CO $_2$, where TEA served as a sacrificial electron donor. Measurements were conducted under visible light (300W Xe lamp, visible bandpass 400–700 nm) to utilize the visible light absorption feature of ReTC. We note this is in contrast to previous work where it relied on the intense absorption at the UV region (300–350 nm) associated with $\pi\text{--}\pi^*$ energy transition of the bipyridine linker 7 . The products were analyzed and quantified using gas chromatography (GC) and normalized to the number of ReTC in Re $_n$ -MOFs to get the turnover number (TON). Photocatalytic CO $_2$ to CO conversion behavior of Re $_n$ -MOFs is shown in Figure 2e, reaching peak activity with Re $_3$ -MOF. In absence of CO $_2$ (under Ar atmosphere) or with no ReTC, there was no CO generation observed. The performance of Re $_n$ -MOFs was stable at least up to 4 hours (Figure S11 in SI) compared to the molecular counterpart 11 , which deactivates within the first hour (Figure S12 in SI). The enhanced stability of Re $_n$ -MOFs is from the covalent attachment of Re centers in ReTC, which prevents the prevailing deactivation pathway of dimerization commonly observed with photoactive molecular complexes (Figure S13-14 in SI). IR spectra of Re $_3$ -MOF before and after

the reaction (Figure S15 in SI) shows that Re_n -MOFs preserve the molecular configuration of *fac*- ReTC after photocatalysis while in comparison the $\nu(\text{CO})$ bands for molecular H_2ReTC are shifted because of dimerization. This clearly indicates the inability of ReTC to dimerize due to its covalent bonding to the MOF in Re_n -MOFs.

2. Effect of the molecular environment within MOFs for photocatalytic CO_2 reduction

IR Spectroscopy of Re_n -MOFs and Molecular H_2ReTC . The photocatalytic trend observed for Re_n -MOFs should be closely related to the configuration of ReTC and its surrounding environment. The vibrational stretching modes of ReTC carbonyl ligands in Re_n -MOFs were probed by IR spectroscopy and compared with those of the molecular H_2ReTC (Figure 3). In the cases of Re_1 -, Re_2 -, and Re_3 -MOFs, $\nu(\text{CO})$ bands were observed at 2,022, 1,920, and 1,910 cm^{-1} , which are identical to the IR spectra of H_2ReTC dispersed in solution. On the other hand, the $\nu(\text{CO})$ bands at lower wavenumbers were shifted to lower frequency for Re_5 -, Re_{11} -, Re_{16} -, and Re_{24} -MOFs. This indicated that there is electron-backdonation to the carbonyl ligand from Re of other ReTC s, weakening the CO bond strength¹². This effect is possibly due to weak interactions between contiguous overlapping ReTC s. This was also observed when H_2ReTC molecules are tightly packed as powder and moistened with acetonitrile, where $\nu(\text{CO})$ bands are shifted to 1,900 and 1,880 cm^{-1} .

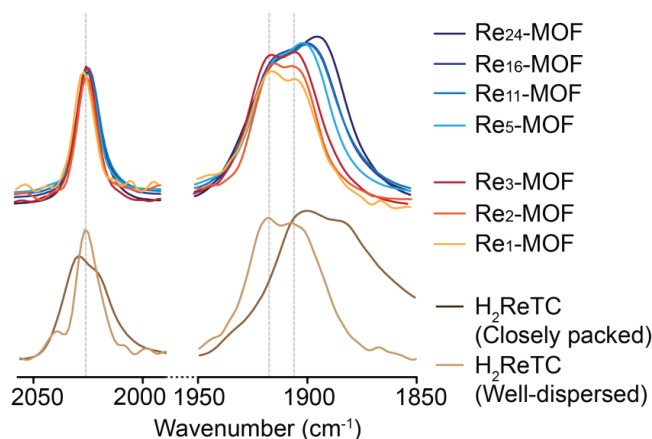


Figure 3. IR spectra of Re_n -MOFs and H_2ReTC .

Re_n -MOFs with n above 4. Considering that ReTC s are observed within the octahedral cavity of Re_3 -MOF from single crystal X-ray diffraction and the axial rotation of the ReTC linker backbone, the maximum number of ReTC units that can be incorporated into Re_n -MOF without overlapping is 4 per unit cell, with each octahedral cavity being occupied with a single ReTC complex (Figure S16 in SI). We believe a statistically variable distribution of ReTC s within the framework is most reasonable to expect. Beyond this point, the likelihood of ReTC s occupying adjacent linkers and hence overlapping increases. Indeed, if the linkers can

rotate 180° into adjacent octahedral cavities, beyond 4 per unit cell there will unavoidably be some ReTC s clashing from this rotation (Figure S17a in SI). The IR spectra are consistent with the unit cell structure considerations where Re_5 -MOF is just beyond the limit of ReTC being undisturbed. Therefore, the excessive occupation of ReTC s in Re_n -MOFs appear to cause a change in their vibrational state¹³, which may not be favorable for reducing CO_2 and decreases activity for Re_n -MOFs with n above 4. Another aspect to note is the accessible pore volume of Re_n -MOFs: N_2 uptake on a volumetric scale (Figure S9 in SI) is lower for frameworks with more than 4 ReTC per unit cell. This indicates that substrate and product diffusion may also be limited within Re_n -MOFs with n above 4, further resulting in the observed lowering of activity.

Re_n -MOFs with n below 4. However, we see an increase in activity in the lower regime of ReTC incorporation, from Re_1 to Re_3 . Though a unimolecular pathway has been reported to exist for molecular ReTC ^{14a}, the observed rise in photocatalytic activity with more ReTC units within Re_n -MOF (n below 4) implies that the bimolecular reaction pathway (bridging or outer-sphere electron transfer) is the source of the higher turnover^{13,14}, which is expected for a reaction involving 2 electrons (Figure S17b and 18 in SI). Therefore, a fine balance of proximity between photoactive centers is needed for such cooperatively enhanced activity. Furthermore, reduced activity compared to the molecular ReTC in solution (Supporting Information Figures 11 and 12) indicates that restricting the free motion of the molecular complex may limit its activity though it is protected from rapid deactivation. The present study of Re_n -MOFs not only elucidates the effect of the molecular environment within MOFs for photocatalytic CO_2 reduction, but also provides further insights into the photocatalytic reaction pathway of molecular ReTC .

3. Plasmon-Enhanced Photocatalytic Activity of Re_n -MOFs

Synthesis and characterization of Re_n -MOFs coated on plasmonic Ag nanocubes. Coupling Re_3 -MOF to a plasmonic Ag nanoparticle was performed to demonstrate an effective strategy in creating a bifunctional catalyst with enhanced activity and long-term stability. The optimal Re_3 -MOF structure with the highest turnover was coated on Ag nanocubes ($\text{Ag}@\text{Re}_3\text{-MOF}$). Once irradiated with light, the Ag nanocubes generate intensified near-surface electric fields at their surface plasmon resonance frequency that can be orders of magnitude higher in intensity than the incident electromagnetic field^{1b, 15}. Therefore, it is expected that Re_3 -MOF coating on the Ag nanocubes can spatially localize photoactive Re centers to the intensified electric fields with enhanced photocatalytic activity. More recently, there have been some examples of combining Au and Ag nanoparticles with MOFs capable of oxidizing alcohols and dyes that led to several-fold enhancement in their performance¹⁶. Ag nanocubes prepared by the polyol process¹⁷ were used in the synthesis procedure of Re_n -MOF to give $\text{Ag}@\text{Re}_3\text{-MOF}$. Figure 4a shows a TEM image of

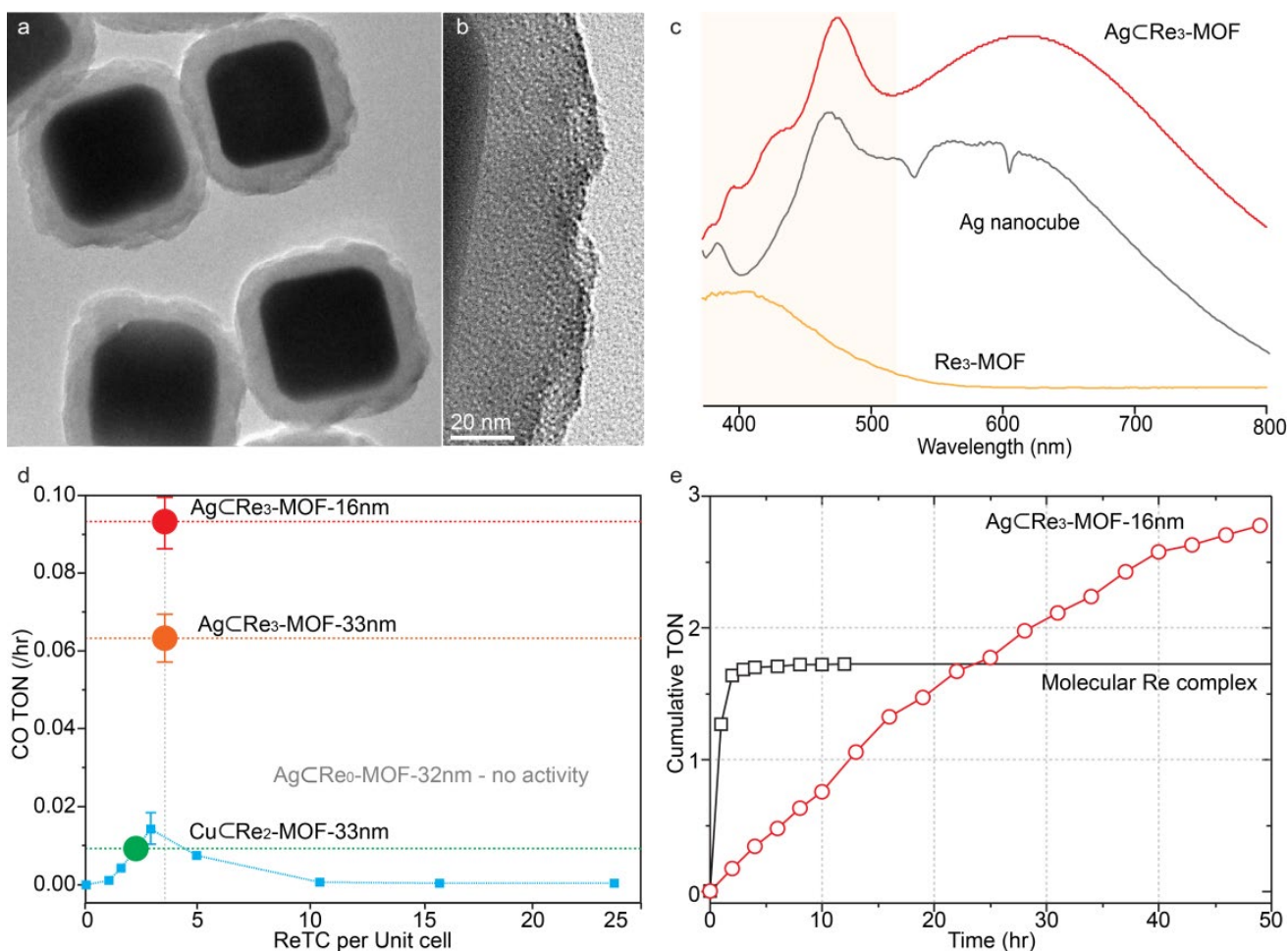


Figure 4. Characterization of Ag@Re₃-MOF. (a) TEM image of Ag@Re₃-MOF showing Re₃-MOF constructed on the surface of a Ag nanocube. (b) Magnified image of Re₃-MOF. (c) UV-Vis spectra of Re₃-MOF, Ag nanocube, and Ag@Re₃-MOF. (d) Photocatalytic CO₂-to-CO conversion activity of Re_n-MOFs, Ag@Re₀-MOF, Cu@Re₂-MOF, and Ag@Re₃-MOFs with MOF thickness of 16 nm and 33 nm. (e) Stable performance of Ag@Re₃-MOF compared to molecular H₂ReTC.

Ag@Re₃-MOF. The dark area in the core is the Ag nanocube (98 nm in diameter) while the brighter outer part is the Re₃-MOF with a thickness of 33 nm. The magnified image of the outer part (Figure 4b) shows lattice fringes from the crystalline Re₃-MOF layer. ICP-AES analysis revealed that the Re₃-MOF layer contains the expected three ReTCs per unit cell. The crystallinity of Ag@Re₃-MOF was examined by PXRD (Figure S19 in SI). The resulting diffraction lines of Ag@Re₃-MOF match those of Ag and Re₃-MOF, indicating the preservation of the Ag metallic phase and the formation of the Re₃-MOF structure on the surface of Ag. The permanent porosity of Ag@Re₃-MOF was confirmed by N₂ sorption (Figure S20 in SI). IR spectroscopy showed that $\nu(\text{CO})$ bands were consistent with those of molecular H₂ReTC and Re₃-MOF (Figure S21 in SI). From the UV-Vis spectrum (Figure 4c), the Ag nanocube exhibits a strong quadrupolar localized surface plasmon resonance (LSPR) scattering peak ($\lambda_{\text{max}} \sim 480\text{nm}$)^{17, 18}, which overlaps with the absorption range of ReTC (400 nm < λ < 550 nm) in the

visible region. Furthermore, the Ag@Re₃-MOF structure retains the characteristic LSPR features of the Ag core after being coated with the Re₃-MOF. Therefore, it is expected that the intensified near-field created at the surface of Ag nanocubes can be absorbed by ReTCs incorporated into the Re₃-MOF layer for photocatalytic enhancement.

Photocatalytic activity and stability of Ag@Re_n-MOFs. Photocatalytic CO₂-to-CO conversion activity of Ag@Re₃-MOF was performed under identical conditions to those expressed above (Figure 4d). As expected, Ag@Re₃-MOF exhibits 5 times enhancement of activity over Re₃-MOF under visible light. Since the intensity of the near-field from LSPR decays exponentially with the distance from the surface of the nanoparticle^{4d}, ReTCs in a thinner MOF layer will be under the influence of a stronger electric field on average, leading to superior turnover. A thinner Re₃-MOF layer (16 nm) was coated on Ag nanocubes by controlling the synthetic conditions (Figure S22 in SI) and this structure provided 7 times further enhancement of

photocatalytic activity (Figure 4d). When there was no ReTC in the MOF layer (i.e. Ag@Re₀-MOF) (Figure S23 in SI), there was no activity observed; ruling out the possibility of Ag being responsible for CO production. Additionally, when Re₂-MOF was coated on Cu nanoparticles of similar size (~100 nm, Figure S24 in SI), activity enhancement was not observed (Figure 4d) as the Cu nanoparticles do not have the LSPR characteristics that match with the absorption features of ReTC (Figure S25 in SI).

The Ag nanocube coated with Re-MOF should not only exhibit enhanced photocatalytic activity but long-term stability as well from having ReTCs covalently bound within the MOF. The stability of the Ag@Re₃-MOF structure was tested by measuring its activity up to 48 hours under visible light (Figure 4e). Compared to molecular H₂ReTC, which rapidly deactivates within the first hour possibly from dimerization as previously reported¹¹, Ag@Re₃-MOF shows stable photocatalytic performance throughout the entire period and its cumulative TON exceeds that of H₂ReTC after 24 hours. The stability of the structure was confirmed with TEM and IR spectroscopy following the long-term measurement (Supporting Information Figures 26 and 27). The CO produced from Ag@Re₃-MOF almost doubled from that of H₂ReTC after 48 hours, demonstrating the combined effects gained from this bifunctional catalyst construct.

SUMMARY

We show how covalently attached photoactive centers within MOF interior can be spatially localized and subjected to the enhanced electromagnetic field surrounding plasmonic silver nanocubes to significantly increase their photocatalytic activity. We covalently attached Re^I(CO)₃(BPYDC)Cl, BPYDC = 2,2'-bipyridine-5,5'-dicarboxylate, into a zirconium MOF, UiO-67, and controlled its density in the pores in increments (0, 1, 2, 3, 5, 11, 16, and 24 complexes per unit cell), which led to observing the highest activity for 3 complexes. This activity trend resulted from the molecular environment within MOFs that varied with ReTC density. Placing the optimal Re₃-MOF structure with the highest turnover on silver nanocubes resulted in seven-fold enhancement of photocatalytic activity under visible light.

ASSOCIATED CONTENT

Supporting Information

Materials and methods, structural analysis of single-crystalline Re₃-MOF, and additional characterization of Re_n-MOF and Ag@Re₃-MOF. This material is available free of charge via the Internet at <http://pubs.acs.org>.

AUTHOR INFORMATION

Corresponding Authors

p_yang@berkeley.edu, yaghi@berkeley.edu.

Author Contributions

The manuscript was written through contributions of all authors. All authors have given approval to the final version of the manuscript. / #These authors contributed equally.

Notes

The authors declare no competing financial interest.

ACKNOWLEDGMENT

The research performed in O.M.Y. laboratory was supported by BASF SE (Ludwigshafen, Germany), and King Abdulaziz City for Science and Technology as part of a joint KACST - UC Berkeley collaboration (Center of Excellence for Nanomaterials and Clean Energy Applications). Financial support for part of this work performed in the P.Y. laboratory was supported by the Director, Office of Science, Office of Basic Energy Sciences, Materials Sciences and Engineering Division, of the U.S. Department of Energy under Contract No. DE-AC02-05CH11231 (Surface). D.K. acknowledges support from Samsung Scholarship and K.M.C. acknowledges support from Basic Science Research Program through the National Research Foundation of Korea (NRF) (2016R1C1B1010781) and Sookmyung Women's University Research Grant (1-1603-2038). Work performed at the Advanced Light Source is supported by the Director, Office of Science, Office of Basic Energy Sciences, of the U.S. Department of Energy under Contract No. DE-AC02-05CH11231. The NMR Work at the Molecular Foundry was supported by the Office of Science, Office of Basic Energy Sciences, of the U.S. Department of Energy under Contract No. DE-AC02-05CH11231. We thank Chenlu Xie and Dr. Tsung Rong for help in the synthesis of Ag nanocubes, and Drs. Wooyeol Kim and Heinz Frei for the use of IR and UV-Vis instruments. Drs. S. Teat and K. Gagnon are acknowledged for the synchrotron X-ray diffraction data acquisition support at the beamline 11.3.1 at Advanced Light Source, Lawrence Berkeley National Laboratory.

REFERENCES

- (1) (a) White, J. L.; Baruch, M. F.; Pander III, J. E.; Hu, Y.; Fortmeyer, I. C.; Park, J. E.; Zhang, T.; Liao, K.; Gu, J.; Yan, Y.; Shaw, T. W.; Abelev, E.; Bocarsly, A. B. *Chem. Rev.* **2015**, *115*, 12888. (b) Berardi, S.; Drouet, S.; Francàs, L.; Gimbert-Suriñach, C.; Guttentag, M.; Richmond, C.; Stoll, T.; Llobet, A. *Chem. Soc. Rev.* **2014**, *43*, 7501.
- (2) (a) Kim, D.; Sakimoto, K. K.; Hong, D.; Yang, P. *Angew. Chem., Int. Ed.* **2015**, *54*, 2. (b) Kumar, B. Llorente, M.; Froehlich, J.; Dang, T.; Sathrum, A.; Kubiak, C. P. *Annu. Rev. Phys. Chem.* **2012**, *63*, 541.
- (3) Furukawa, H.; Cordova, K. E.; O'Keeffe, M.; Yaghi, O. M. *Science* **2013**, *341*, 974.
- (4) (a) Hou, W.; Hung, W. H.; Pavaskar, P.; Goepfert, A.; Aykol, M.; Cronin, S. B. *ACS Catal.* **2011**, *1*, 929. (b) Hou, W.; Cronin, S. B. *Adv. Funct. Mater.* **2013**, *23*, 1612. (c) Tu, W.; Zhou, Y.; Li, H.; Li, P.; Zou, Z. *Nanoscale* **2015**, *7*, 14232. (d) Yuan, Y.-P.; Ruan, L.-W.; Barber, J.; Loo, S. C. J.; Xue, C. *Energy Environ. Sci.* **2014**, *7*, 3934.
- (5) Cavka, J. H.; Jakobsen, S.; Olsbye, U.; Guillou, N.; Lamberti, C.; Bordiga, S.; Lillerud, K. P. *J. Am. Chem. Soc.* **2008**, *130*, 13850.
- (6) (a) Smieja, J. M.; Benson, E. E.; Kumar, B.; Grice, K. A.; Seu, C. S.; Mille, A. J. M.; Mayer, J. M.; Kubiak, C. P. *Proc. Natl. Acad. Sci. U S A.* **2012**, *109*, 15646. (b) Morris, A. J.; Meyer, G. J.; Fujita, E. *Acc. Chem. Res.* **2009**, *42*, 1983.
- (7) (a) Wang, C.; Xie, Z.; deKrafft, K. E.; Lin, W. *J. Am. Chem. Soc.* **2011**, *133*, 13445. (b) Blake, A. J.; Champness, N. R.; Easun, T. L.; Allan, D. R.; Nowell, H.; George, M. W.; Jia, J.; Sun, X.-Z. *Nat. Chem.* **2010**, *2*, 688.
- (8) (a) Chambers, M.B.; Wang, X.; Elgrishi, N.; Hendon, C. H.;

- Walsh, A.; Bonnefoy, J.; Canivet, J.; Quadrelli, E. A.; Farrusseng, D.; Mellot-Draznieks, C.; Fontecave, M. *ChemSusChem*. **2015**, *8*, 603. (b) Lee, Y.; Kim, S.; Kang, J. K.; Cohen, S. M. *Chem. Commun.* **2015**, *51*, 5735. (c) Fei, H.; Sampson, M. D.; Lee, Y.; Kubiak, C. P.; Cohen, S. M. *Inorg. Chem.* **2015**, *54*, 6821. (d) Fu, Y.; Sun, D.; Chen, Y.; Huang, R.; Ding, Z.; Fu, X.; Li, Z. *Angew. Chem. Int. Ed.* **2012**, *51*, 3364. (e) Wang, D.; Huang, R.; Liu, W.; Sun, D.; Li, Z. *ACS Catal.* **2014**, *4*, 4254. (f) Wang, S.; Yao, W.; Lin, J.; Ding, Z.; Wang, X. *Angew. Chem. Int. Ed.* **2014**, *53*, 1034. (g) Huang, R.; Peng, Y.; Wang, C.; Shi, Z.; Lin, W. *Eur. J. Inorg. Chem.* **2016**, *27*, 4358. (h) Easun, T. L.; Jia, J.; Calladine, J. A.; Blackmore, D. L.; Stapleton, C. S.; Vuong, K. Q.; Champness, N. R.; George, M. W. *Inorg. Chem.*, **2014**, *53*, 2606.
- (9) (a) Liang, Y. T.; Vijayan, B. K.; Gray, K. A.; Hersam, M. C. *Nano Lett.* **2011**, *11*, 2865. (b) Neațu, Ș.; Maciá-Agulló, J. A.; Concepción, P.; Garcia, H. *J. Am. Chem. Soc.* **2014**, *136*, 15969. (c) Ma, Y.; Wang, X.; Jia, Y.; Chen, X.; Han, H. Li, C. *Chem. Rev.* **2014**, *114*, 9987. (d) Liang, W.; Church, T. L.; Zheng, S.; Zhou, C.; Haynes, B. S.; D'Alessandro, D. M. *Chem. Eur. J.* **2015**, *21*, 18576.
- (10) Sato, S.; Morimoto, T.; Ishitani, O. *Inorg. Chem.* **2007**, *46*, 9051.
- (11) Benson, E. E.; Kubiak, C. P. *Chem. Commun.* **2012**, *48*, 7374.
- (12) Zhao, H. C.; Mello, B.; Fu, B. L.; Chowdhury, H.; Szalda, D. J.; Tsai, M. K.; Grills, D. C.; Rochford, J. *Organometallics* **2013**, *32*, 1832.
- (13) Hayashi, Y.; Kita, S.; Brunschwig, B. S.; Fujita, E. *J. Am. Chem. Soc.* **2003**, *125*, 11976.
- (14) (a) Gibson, D. H.; Yin, X.; He, H.; Mashuta, M. S. *Organometallics* **2003**, *22*, 337. (b) Gibson, D. H.; Yin, X. *J. Am. Chem. Soc.* **1998**, *120*, 11200. (c) Takeda, H.; Koike, K.; Inoue, H.; Ishitani, O., *J. Am. Chem. Soc.* **2008**, *130*, 2023. (d) Meister, S.; Reithmeier, R. O.; Tschurl, M.; Heiz, U.; Rieger, B. *ChemCatChem*, **2015**, *7*, 690.
- (15) Linic, S.; Christopher, P.; Ingram, D. B. *Nat. Mater.* **2011**, *10*, 911.
- (16) (a) Yuan, X.; Wang, H.; Wu, Y.; Zeng, G.; Chen, X.; Leng, L.; Wu, Z.; Li, H. *Appl. Organometal. Chem.* **2016**, *30*, 289. (b) Gu, Z.; Chen, L.; Duan, B.; Luo, Q.; Liu, J.; Duan, C. *Chem. Commun.* **2016**, *52*, 116. (c) Gao, S.-T.; Liu, W.-H.; Shang, N.-Z.; Feng, C.; Wu, Q.-H.; Wang, Z.; Wang, C. *RSC Adv.* **2014**, *4*, 61736.
- (17) Tao, A.; Sinsermsuksakul, P.; Yang, P. *Angew. Chem. Int. Ed.* **2016**, *45*, 4597.
- (18) Wu, H.-J.; Henzie, J.; Lin, W.-C.; Rhodes, C.; Li, Z. Sartorel, E.; Thorner, J.; Yang, P.; Groves, J. T. *Nat. Methods* **2012**, *9*, 1189.

